



Theoretical study of microcavity-enhanced absorption spectroscopy for mid-infrared methane detection using a chalcogenide/silica-on-fluoride horizontal slot-waveguide racetrack resonator

MINGQUAN PI,¹ CHUANTAO ZHENG,^{1,*}  ZIHANG PENG,¹ HUAN ZHAO,¹ JIAMING LANG,¹ LEI LIANG,² YU ZHANG,¹ YIDING WANG,¹ AND FRANK K. TITTEL³

¹State Key Laboratory of Integrated Optoelectronics, College of Electronic Science and Engineering, Jilin University, 2699 Qianjin Street, Changchun 130012, China

²State Key Laboratory of Luminescence and Applications, Changchun Institute of Optics Fine Mechanics and Physics, Chinese Academy of Sciences, Changchun 130033, China

³Department of Electrical and Computer Engineering, Rice University, 6100 Main Street, Houston, TX 77005, USA

*zhengchuantao@jlu.edu.cn

Abstract: The reported chalcogenide (ChG) rectangular waveguide sensors with a small evanescent field need a large waveguide length to obtain an enhanced light-gas interaction effect. To make such sensors compact and improve the light-gas interaction effect, a microcavity-enhanced absorption spectroscopy technique for methane (CH₄) detection was proposed using a mid-infrared chalcogenide/silica-on-fluoride horizontal slot-waveguide racetrack resonator. For the horizontal slot waveguide, an equivalent sensor model (ESM) and related formulations were proposed to simplify the analysis of the racetrack resonator sensor model (RRSM), and the ESM was verified through a comparison between the theoretical result of ESM and the simulation result of RRSM based on the finite element method (FEM). Due to the use of a chalcogenide/silica-on-fluoride horizontal slot-waveguide structure, the waveguide parameters were optimized to obtain a high power confinement factor of 44.63% at the wavelength of 3291 nm, which is at least 5 times higher than other ChG rectangular waveguides. The waveguide length is reduced at least 30 times due to the use of the optimized chalcogenide/silica-on-fluoride horizontal slot-waveguide and racetrack resonator. The limit of detection (LoD) is 3.87 ppm with an intrinsic waveguide loss of 3 dB/cm and an amplitude coupling ratio of 0.1 for the resonator. The response time is less than 5 μs due to the small light-gas interaction area. The influences of environmental pressure and waveguide intrinsic loss on the sensing characteristics were discussed. The compact racetrack resonator sensor structure and equivalent analytical model can also be adopted in the design of an on-chip waveguide sensor for the detection of other gas species.

© 2020 Optical Society of America under the terms of the [OSA Open Access Publishing Agreement](#)

1. Introduction

Most gas species have unique absorption in the mid-infrared band (2.5–20 μm), and the absorption intensity is at least two orders larger than that in the near-infrared band. However, the reported mid-infrared gas sensor systems based on discrete modules or devices with bulk size are power-consuming and sensitive to vibration [1–9]. Some other gas sensing techniques (e.g., electrochemical, catalysis) require a high operation temperature (> 200°C) for activating functional materials [10]. As a comparison with the discrete sensor system, a chip-scale optical waveguide gas sensor is mini in size with small power consumption [11–13]. Moreover, optical

waveguide sensors can be used for label-free, non-invasive and non-damage sensing [14–15]. Based on refractive index variation or absorption spectroscopy, solid, liquid and gaseous analyte can be qualitatively or quantitatively analyzed using optical waveguide sensors [16–18].

Waveguide material and structure are two major considerations in the design of an optical waveguide sensor. Waveguide material should be transparent in the mid-infrared to reduce absorption loss. Chalcogenide (ChG) glasses with a high refractive index (> 2) have a low absorption loss below $12\ \mu\text{m}$ [19], which are suitable as core layer material. Calcium fluoride (CaF_2) with a low refractive index (~ 1.4) has low absorption loss below $9\ \mu\text{m}$ [20], which is suitable as lower buffer layer material. The widely used silicon-on-insulator (SOI) platform is unsuitable for mid-infrared applications because the transparent waveband of the silica (SiO_2) is limited to $\sim 3.6\ \mu\text{m}$ [21]. On the other hand, waveguide structure should have a high power confinement factor (PCF) within the target gas area for strong light-gas interaction. The easily fabricated rectangular waveguide is the most commonly used structure, but its PCF is $< 10\%$ [19,22–23]. To solve this problem, horizontal slot waveguide was proposed to reduce scattering loss and obtain a high PCF [20,24]. Using wet etching technique, horizontal slot waveguide is easy to fabricate without considering the depth-to-width ratio of the slot. In addition, spiral and flexural waveguide structures were proposed to achieve large interaction length with a compact size [25–26]. Superior to spiral and flexural waveguide structures, optical microring resonator is capable of shortening the device length by at least 10 times by enabling light circling in the ring microcavity [27].

In order to obtain a large light-gas interaction length, a novel mid-infrared ChG/silica-on-fluoride horizontal slot-waveguide racetrack resonator gas sensor was proposed, which reveals a high PCF of $> 40\%$ and a reduction in the device length by > 30 times. The novel aspects of this racetrack resonator gas sensor include: (1) Instead of vertical slot-waveguide based on dry-etching technique, horizontal slot-waveguide was adopted to obtain a high PCF as well as a low scattering loss due to wet-etching technique. (2) SiO_2 near the horizontal slot was removed by hydrofluoric acid (HF) to reduce absorption loss and enhance the light-gas interaction for dropping the limit of detection (LoD). (3) An equivalent sensor model (ESM) and related formulations were proposed to simplify the analysis of the racetrack resonator sensor model (RRSM), and the ESM was verified through a comparison between the theoretical result of the ESM and the simulation result on the RRSM using COMSOL Multiphysics. The structural parameters of the horizontal slot waveguide and racetrack resonator were optimized for improving the PCF and reducing the sensor size. Methane (CH_4) was selected as the target gas to estimate the sensing characteristics of the racetrack resonator gas sensor. Effects of operation temperature, environmental pressure and waveguide intrinsic loss on the sensor behavior were discussed to prove the robustness of the ChG/silica-on-fluoride horizontal slot-waveguide racetrack resonator.

2. ChG/silica-on-fluoride horizontal slot-waveguide

2.1. Waveguide structure

CH_4 is selected as the target gas and the absorption line located at $\lambda = 3291\ \text{nm}$ is used as the target line for detection [28]. The structure of the proposed ChG/silica-on-fluoride horizontal slot-waveguide is shown in Fig. 1(a). The waveguide consists of an upper confined layer, an upper loaded strip core layer, a supporting layer, a horizontal slot, a lower strip core layer, and a lower buffer layer/substrate. The ChG material, As_2Se_3 is used as the core material with a refractive index $n_1 = 2.80$ (@ $25\ ^\circ\text{C}$) at the wavelength of $3291\ \text{nm}$. SiO_2 is adopted as the supporting layer, and the SiO_2 near the slot is removed for PCF enhancement and decreasing the absorption loss by keeping it away from the slot. Then the effects of the supporting layer on the mode can be neglected. The fluoride material, CaF_2 is used as the lower buffer layer as well as the substrate with a refractive index $n_2 = 1.41$ (@ $25\ ^\circ\text{C}$). The target gas, with a refractive index of $n_3 = 1.0$, is filled in the horizontal slot and used as the upper confined layer above the upper loaded strip. The

waveguide parameters include the upper loaded strip width w_1 , upper strip height h_1 , suspended waveguide width w_2 , suspended waveguide height h_2 , slot height h_3 , and lower strip height h_4 . In the next, the slot waveguide structure will be optimized for guiding single-mode propagation and enhancing PCF in the target gas area.

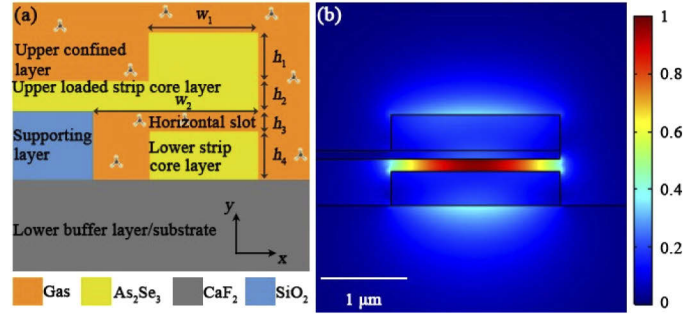


Fig. 1. (a) The cross-section structure of the horizontal slot-waveguide. (b) Optical mode field distribution of the quasi-TM₀ mode of horizontal slot-waveguide, where $w_1 = 2 \mu\text{m}$, $w_2 = 6 \mu\text{m}$, $h_1 = 0.42 \mu\text{m}$, $h_2 = 0.1 \mu\text{m}$, $h_3 = 0.15 \mu\text{m}$, and $h_4 = 0.4 \mu\text{m}$.

2.2. Waveguide cross-section optimization

There are two goals for optimizing the ChG/silica-on-fluoride horizontal slot-waveguide racetrack resonator. One goal is to meet the single-mode condition with increasing the PCF. The other goal is to increase the effective path length L_{eff} and reduce the waveguide length. Here, COMSOL Multiphysics was used for analysis based on the finite element method (FEM). The PCF within the target gas area is defined as

$$PCF = \frac{\iint_{\text{gas}} P_z dx dy}{\iint_{\text{total}} P_z dx dy} \quad (1)$$

where P_z is the z component of the Poynting vector.

Table 1. Optimized parameters of the ChG/silica-on-fluoride horizontal slot-waveguide.

Slot-waveguide parameters	Value
Wavelength, λ	3291 nm
Upper loaded strip width, w_1	2 μm
Suspended waveguide width, w_2	6 μm
Upper strip height, h_1	0.42 μm
Suspended waveguide height, h_2	0.1 μm
Slot height, h_3	0.15 μm
Lower strip height, h_4	0.4 μm
Racetrack resonator parameters	Value
Radius of racetrack waveguide, r	108 μm
Straight waveguide length of racetrack waveguide, L_1 Straight waveguide length, $2L_2$ Coupling distance, d	16 μm 232 μm 1.5 μm
Performance	Value
Effective refractive index, N_{eff}	1.5925
Power confinement factor, PCF Amplitude coupling ratio, κ	44.63% 0.1

For the quasi- TM_0 mode of the straight horizontal slot-waveguide, we optimized the upper strip, the slot and the lower strip in turn to increase PCF with the same method in our previous work [28]. The optimized results of the slot waveguide parameters are shown in Table 1, where $w_1 = 2 \mu\text{m}$, $w_2 = 6 \mu\text{m}$, $h_1 = 0.42 \mu\text{m}$, $h_2 = 0.1 \mu\text{m}$, $h_3 = 0.15 \mu\text{m}$ and $h_4 = 0.4 \mu\text{m}$. The effective refractive index N_{eff} and PCF of the ChG/silica-on-fluoride horizontal slot-waveguide are 1.5925 and 44.63%, respectively. With the optimized structure, the mode field distribution of the quasi- TM_0 mode of the horizontal slot waveguide is shown in Fig. 1(b). It can be found that a large amount of light is distributed in the target gas area to improve the sensing performance.

3. Horizontal slot-waveguide racetrack resonator gas sensor

3.1. Sensor structure

The top view of the horizontal slot-waveguide racetrack resonator sensor is shown in Fig. 2(a). The output power from the drop port is used for gas detection. The following parameters should be optimized for small bending loss α_b and large effective path length L_{eff} , including the straight waveguide length of the racetrack waveguide L_1 , the radius of the racetrack waveguide r , the coupling distance d , the straight waveguide length L_2 , the amplitude coupling ratio κ and the amplitude transmission ratio t . The system-level diagram of the horizontal slot-waveguide racetrack resonator sensor is shown in Fig. 2(b). A commercially available interband cascade laser (ICL, TO66, Nanoplus, Germany) can be used as the mid-infrared laser with an output power P_0 . The waveguide can easily be butt coupled using fluoride fibers. A single mode fluoride fiber (Thorlabs, ZrF₄ fiber patch cable) can be used to couple the incident light into the waveguide. The output light of the waveguide can be coupled by multimode fluoride fiber (Thorlabs, InF₃ fiber patch cable). The coupling loss of each facet is considered to be 5 dB, which refers to the simulation results of a horizontal rib slot waveguide [20]. The output laser power P from the drop port is derived by a HgCdTe detector (PDA10JT, Thorlabs, USA) with a specific noise equivalent power (NEP) and bandwidth B . The signal output from the detector is processed by an electrical circuit board (ECB). A data acquisition (DAQ) card (USB6211, National Instrument, USA) is used to sample the output signal from the detector and deliver a signal to drive the ICL. Two temperature controllers (TC1, TC2) are used to control the temperature of the laser and waveguide sensor, respectively. A current driver (CD) is used to control the current and to tune the laser wavelength. A laptop as well as a LabVIEW platform is used for data processing and control the DAQ card. For sensing application, a polydimethylsiloxane (PDMS) gas cell can be bonded on the integrated sensor. An inlet and outlet are added to the PDMS gas cell, and the injection and ejection of the target gas into the waveguide can be realized through a pump.

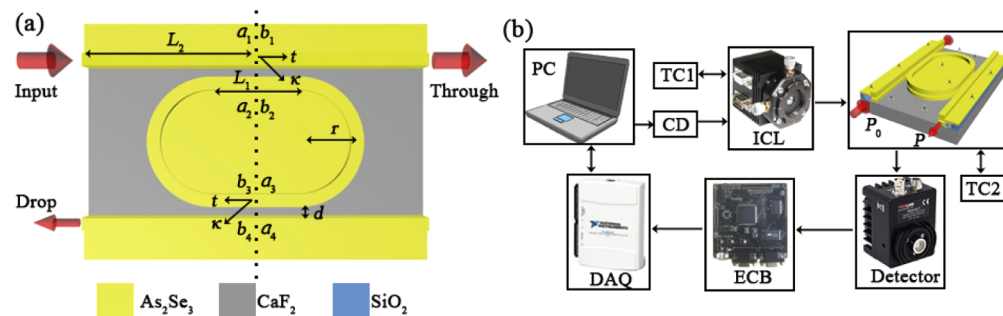


Fig. 2. (a) Top view of the horizontal slot-waveguide racetrack resonator gas sensor. (b) The system-level diagram of the horizontal slot-waveguide racetrack resonator gas sensor. ICL: interband cascade laser; TC: temperature controller; DAQ: data acquisition card; CD: current driver; ECB: electrical circuit board; PC: personal computer.

3.2. Sensing theory

3.2.1. Effective path length

Define b_4 and a_1 as the mode field amplitude of the input straight waveguide and output straight waveguide, respectively. The amplitude transfer function of the racetrack waveguide is determined by the amplitude coupling ratio κ and the amplitude transmission ratio t , shown as

$$\frac{b_4}{a_1} = -\frac{\kappa^2 \exp(-j\varphi)}{1 - t^2 \exp(-j2\varphi)} \quad (2)$$

where $\varphi = L_r[\beta - j(PCF\alpha_{\text{gas}}(C) + \alpha_{\text{int}})]/2$ is the phase change of the light propagating through the semi racetrack waveguide, L_r is the perimeter of the racetrack waveguide, β is the mode propagation constant, α_{int} is the intrinsic loss of the waveguide, including absorption loss, bending loss and scattering loss, $\alpha_{\text{gas}}(C)$ is the waveguide absorption coefficient resulting from the absorption of the target gas at a specific concentration C . At resonance state, the racetrack resonator should satisfy the resonance condition, i.e.

$$L_r\beta = 2\pi m \quad (3)$$

where m is the resonance order. According to Eqs. (2) and (3), the power transfer function of the racetrack waveguide can be written as

$$D_1(C) = \left| \frac{b_4}{a_1} \right|^2 = \left| \frac{\kappa^2 \exp[-L_r(PCF\alpha_{\text{gas}}(C) + \alpha_{\text{int}})/2]}{1 - t^2 \exp[-L_r(PCF\alpha_{\text{gas}}(C) + \alpha_{\text{int}})]} \right|^2 \quad (4)$$

When the analyte is pure nitrogen (N_2), $\alpha_{\text{gas}}(C) \approx 0$, and the power transfer function of the racetrack waveguide can be written as

$$D_0 = \left| \frac{b_4}{a_1} \right|^2 = \left| \frac{\kappa^2 \exp(-L_r\alpha_{\text{int}}/2)}{1 - t^2 \exp(-L_r\alpha_{\text{int}})} \right|^2 \quad (5)$$

Because of light-gas interaction, the output power from the drop port of the racetrack resonator changes with gas concentration and obeys the Lambert-Beer law [22]

$$I = I_0 \exp[-PCF\alpha_{\text{gas}}(C)L_{\text{eff}} - \alpha_{\text{int}}L_{\text{eff}}] \quad (6)$$

where I_0 and I are the output light intensity of the laser and from the drop port, respectively. Since the output power from the drop port P and the laser power P_0 correspond to I and I_0 , respectively, we have

$$P = P_0 D_0 \exp[-PCF\alpha_{\text{gas}}(C)L_{\text{eff}}] \quad (7)$$

On another aspect, based on resonance mode theory, the output power from the drop port can also be expressed as

$$P = P_0 D_1(C) \quad (8)$$

Combining Eqs. (7) and (8), the effective path length L_{eff} of the racetrack waveguide can be decided by

$$L_{\text{eff}} = -\frac{\ln[D_1(C)/D_0]}{PCF\alpha_{\text{gas}}(C)} \quad (9)$$

Considering the length of input/output straight waveguide of the sensor, the total effective path length L_t of the racetrack resonator gas sensor is

$$L_t = 2L_2 + L_{\text{eff}} \quad (10)$$

To make the device compact, the minimum value of L_2 is $L_2 = r + L_1/2$. Then L_t can be written as

$$L_t = 2r + L_1 + L_{\text{eff}} \quad (11)$$

3.2.2. ESM and verification

With the obtained L_{eff} from Section 3.2.1, the RRSM in Fig. 3(a) can be equivalent to a straight waveguide sensor model (ESM) as shown in Fig. 3(b). The straight waveguide sensor is made up of an input straight waveguide, an output straight waveguide and the equivalent straight waveguide for gas sensing. For the two sensor models, the output power can be calculated using Eq. (7) and COMSOL Multiphysics, respectively, to check the accuracy of the equivalent model and theory. The input power of the sensor is set to 10 mW and the waveguide loss only originates from gas absorption. Based on the optimization in Section 2, the racetrack waveguide structural parameters are $r = 108 \mu\text{m}$, $L_1 = 16 \mu\text{m}$ and $d = 1.5 \mu\text{m}$. Curves of the output power P versus CH_4 concentration C for the two models are shown in Fig. 3(c). As can be seen, the output power of the ESM shows good agreement in variation trend with that of the RRSM, and the slight difference probably results from the errors in reducing the three-dimensional waveguide model to two-dimensional waveguide model. This confirms the accuracy of the ESM.

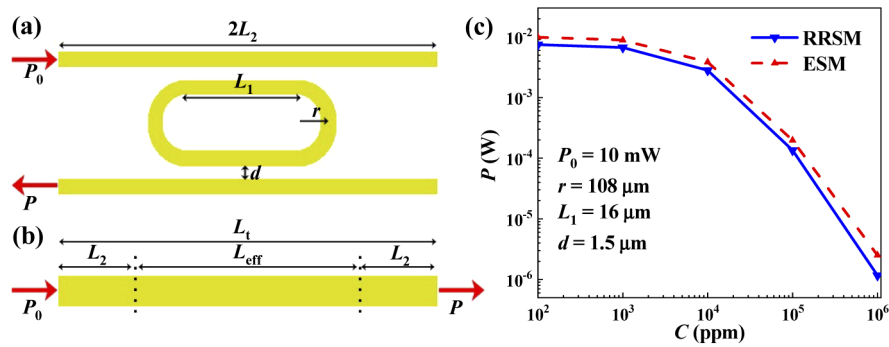


Fig. 3. (a) Racetrack resonator sensor model (RRSM). (b) Equivalent straight waveguide sensor model (ESM). (c) Curves of output power P versus CH_4 concentration C using the two models shown in Fig. 3(a) and 3(b), where $P_0 = 10 \text{ mW}$, $r = 108 \mu\text{m}$, $L_1 = 16 \mu\text{m}$ and $d = 1.5 \mu\text{m}$.

3.2.3. Key characteristics: dynamic range and limit of detection

With the verified ESM (Fig. 3(b)), we can analyze the key characteristics of the sensor using a similar technique proposed in [28]. The LoD satisfies

$$SNR_{\min} NEP \sqrt{B} = P_0 \exp(-\alpha_{\text{int}} L_t) - P_0 \exp[-\alpha_{\text{int}} L_t - PCF \alpha_{\text{gas}} (C = LoD) L_t] \quad (12)$$

where SNR_{\min} as the minimum detectable signal-to-noise ratio of the system, which is related to the detector and electrical units. The C_{\max} satisfies

$$SNR_{\min} NEP \sqrt{B} = P|_{C_{\max}} = P_0 \exp[-\alpha_{\text{int}} L_t - PCF \alpha_{\text{gas}} (C = C_{\max}) L_t] \quad (13)$$

3.3. Sensor optimization

Now we optimize the racetrack waveguide sensor with the optimized waveguide structure in Section 2. Curves of the refractive index difference between the straight waveguide and the bending waveguide ΔN_{eff} and waveguide bending loss α_b versus ring radius r are shown in Fig. 4(a). With the increase of r , ΔN_{eff} and α_b decrease first and then become stable. ΔN_{eff} equals zero when $r > 20 \mu\text{m}$, and the α_b of a typical SOI bending waveguide with $r > 5 \mu\text{m}$ can be ignored [29]. This is because the PCF of the proposed waveguide is large, so a large radius is required for the racetrack resonator waveguide to confine the mode propagation along the waveguide.

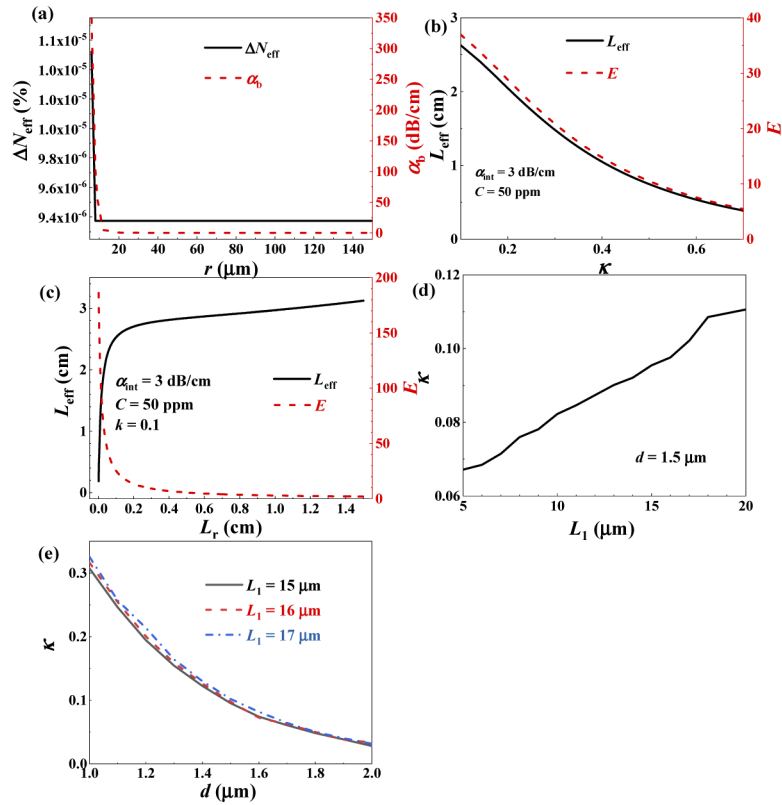


Fig. 4. (a) Curves of ΔN_{eff} and α_b versus r . (b) Curves of L_{eff} and E versus κ where $\alpha_{\text{int}} = 3 \text{ dB/cm}$ and $C = 50 \text{ ppm}$. (c) Curves of L_{eff} and E versus L_r , where $\alpha_{\text{int}} = 3 \text{ dB/cm}$, $C = 50 \text{ ppm}$ and $\kappa = 0.1$. (d) Curves of κ versus L_1 , where $d = 1.5 \mu\text{m}$. (e) Curves of κ versus d at different L_1 from $15 \mu\text{m}$ to $17 \mu\text{m}$.

The micro-cavity enhancement factor is defined as E , which is expressed as $E = L_{\text{eff}} / L_r$. Curves of L_{eff} and E versus mode amplitude coupling ratio κ are shown in Fig. 4(b), where $\alpha_{\text{int}} = 3 \text{ dB/cm}$ and $C = 50 \text{ ppm}$. κ determines the coupling effect between the straight waveguide and racetrack waveguide. When κ is small, light tends to circulate in the racetrack waveguide. So L_{eff} and E decrease with the increase of κ . However, if κ is < 0.1 , it will be difficult for the coupling between the straight waveguide and racetrack waveguide. So we select $\kappa = 0.1$ to obtain a large L_{eff} and a large E . Curves of L_{eff} and E versus L_r are shown in Fig. 4(c), where $\alpha_{\text{int}} = 3 \text{ dB/cm}$, $C = 50 \text{ ppm}$ and $\kappa = 0.1$. With the increase of L_r , L_{eff} increases due to the increased light-gas interaction length. Because of the increased mode loss mainly resulting from α_{int} other than gas absorption, L_{eff} increases more slowly than L_r which leads to the decrease of E . In order to ignore the influence of α_b and achieve a large L_{eff} and E , L_r is selected to be $710 \mu\text{m}$ (a ring waveguide with the radius of $\sim 110 \mu\text{m}$).

Finally, we optimize L_1 to ensure $\kappa = 0.1$. Increasing PCF and L_1 will improve the coupling effect, and the microring resonator can be fabricated without electron beam lithography when the coupling distance $d > 1 \mu\text{m}$. Curve of κ versus L_1 is shown in Fig. 4(d), where $d = 1.5 \mu\text{m}$. As can be seen, κ increases with the increase of L_1 . Curves of κ versus d at different L_1 from $15 \mu\text{m}$ to $17 \mu\text{m}$ are shown in Fig. 4(e). It can be seen that κ decreases with the increase of d because the increase of d weakens the interaction between waveguides. A larger L_1 can enhance the interaction between waveguides which leads to the increase of κ . With increasing L_1 , d can

be decreased to keep κ unchanged; however, the increase of L_1 makes the footprint of the device large. A small d increases the difficulty of device fabrication, and so d is set to 1.5 μm . When $L_1 = 16 \mu\text{m}$, $r = 108 \mu\text{m}$ and $d = 1.5 \mu\text{m}$, κ reaches 0.1. The optimized parameters of the racetrack resonator sensor are shown in Table 1.

3.4. Wavelength tuning characteristics of the optimized resonator

The transmittance spectrum of the drop port is shown in Fig. 5 for the optimized waveguide sensor with an operation temperature of 25 $^{\circ}\text{C}$. The resonance wavelength is near the absorption peak at 3291 nm selected for CH_4 detection.

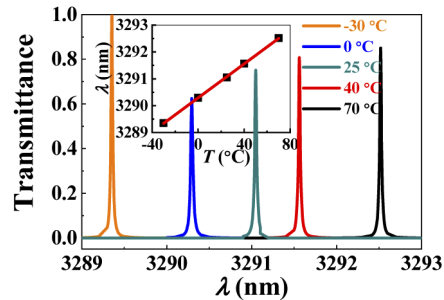


Fig. 5. Curves of resonant peaks of the racetrack resonator at different temperatures. Inset: The thermal-optical tuning coefficient ($d\lambda/dT$) fitting curve.

The refractive indices of waveguide materials are influenced by temperature, so the resonant peak can be tuned to the absorption peak by controlling the temperature of the sensor. The thermo-optic coefficient (dn/dT) of As_2Se_3 and CaF_2 are $\sim 4 \times 10^{-5} \text{ }^{\circ}\text{C}^{-1}$ and $\sim -8.2 \times 10^{-6} \text{ }^{\circ}\text{C}^{-1}$, respectively [28,30]. Assuming that the temperature of the waveguide and substrate is uniform, within the temperature range from $-30 \text{ }^{\circ}\text{C}$ to $70 \text{ }^{\circ}\text{C}$, curves of the resonant peaks at different temperature are shown in Fig. 5. The resonant peak has a red shift with the increase of T . Fitted by least square method, the thermo-optic tuning coefficient ($d\lambda/dT$) is only $\sim 0.032 \text{ nm}/^{\circ}\text{C}$ due to the low thermo-optic coefficient of the core layer. The obtained fitting curve is shown in the inset of Fig. 5. The full width at half maximum (FWHM) of the resonant peak is $\sim 0.03 \text{ nm}$. The simulated absorption spectra of CH_4 and H_2O from HITRAN database are shown in Fig. 6(a), where $T = 298 \text{ K}$, $P = 1 \text{ atm}$, $L = 10 \text{ cm}$ and the concentration of CH_4 and H_2O are 1000 ppm and 2% (atmospheric concentration level), respectively. The influence of H_2O can be ignored by drying the injected gas [1]. The FWHM of the CH_4 absorption peak is $\sim 0.14 \text{ nm}$ which is 4 times larger than the FWHM of the resonant peak. Setting the temperature to 27.5 $^{\circ}\text{C}$, the resonant peak can be located at the CH_4 absorption peak wavelength. The ICL emission spectrum measured by Fourier transform infrared (FTIR) spectrometer (Thermo Fisher Scientific, model Nicolet iS50) is shown in Fig. 6(b), where $T = 15 \text{ }^{\circ}\text{C}$. The output wavelength of the ICL can be located at the CH_4 absorption peak wavelength by adjusting current. The line width of the ICL is narrower than the FWHM of resonant peak and the FWHM of CH_4 absorption peak. So the $\alpha_{\text{gas}}(C)$ of the CH_4 absorption peak can be approximated as a fixed value for theoretical calculation and simulation study.

3.5. Fabrication process

A diagram of the fabrication process of the integrated sensor is shown in Fig. 7. First, a 0.4 μm thick SiO_2 film is deposited on CaF_2 substrate by chemical vapor deposition (CVD). The mask on partial SiO_2 is formed by photolithography and the SiO_2 supporting layer is obtained by inductively coupled plasma (ICP) etching. Then, a ChG strip with a width of 2 μm and a height

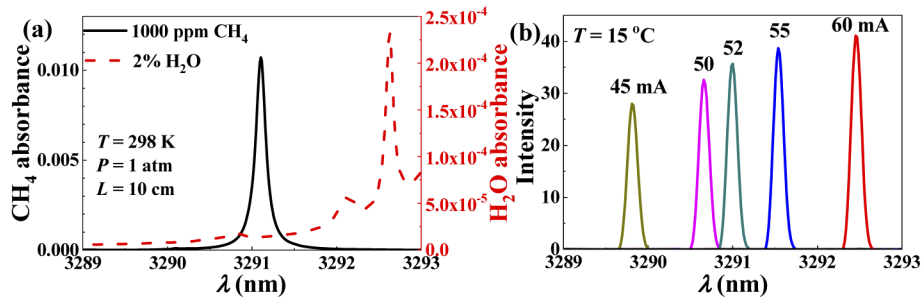


Fig. 6. (a) The simulated absorption spectra of CH₄ and H₂O, where $T = 298$ K, $P = 1$ atm, $L = 10$ cm and the concentration of CH₄ and H₂O are 1000 ppm and 2%, respectively. (b) The ICL emission spectrum measured by Fourier transform infrared (FTIR) spectrometer, where $T = 15$ °C.

of 0.4 μm is fabricated by lift-off technique. Next, a 0.15 μm thick SiO₂ film is fabricated on ChG by CVD. In the following, a 0.52 μm thick ChG film is fabricated on SiO₂ by thermal evaporation and the air groove of the coupling region with a 1.5 μm width is formed by ICP etching. The ChG racetrack disk and strips with a height of 0.42 μm are removed by ICP etching. Finally, the SiO₂ slot is removed by HF etching and the etching rate can be 100 nm/min by controlling the HF concentration and temperature. The suspended width of the ChG microcavity can be < 10 μm [31] and a pedestal waveguide similar to the suspended waveguide is proposed for liquid sensing [32], so the ChG layers can be held up well after the HF etching and the suspended slot waveguide structure can be as stable as the conventional rectangular waveguide and the vertical slot waveguide. Because the coupling distance with a width of 1.5 μm can be reached without electron beam lithography, this kind of racetrack resonator can be fabricated in large scale.

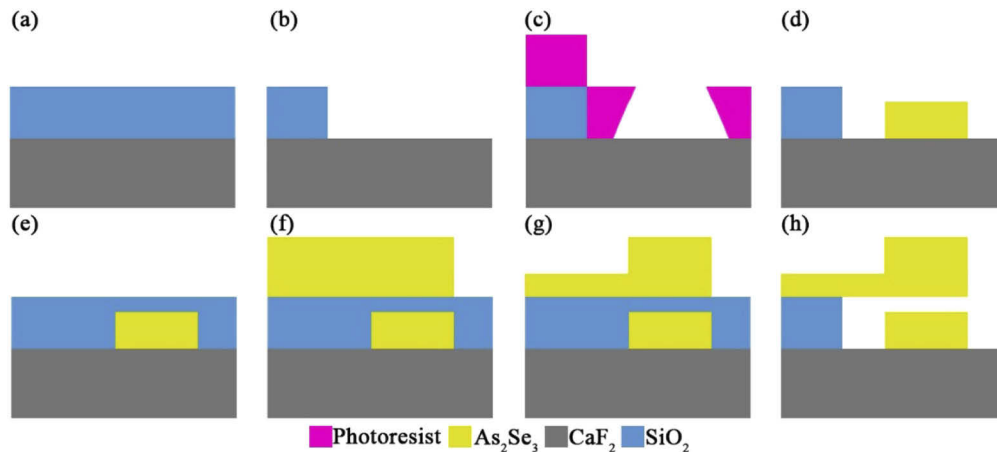


Fig. 7. Fabrication process of the waveguide sensor. (a) Depositing SiO₂ film. (b) Etching SiO₂. (c) Fabricating photoresist mask. (d) Depositing ChG film and removing photoresist. (e) Depositing SiO₂ film. (f) Depositing and etching ChG film. (g) Etching ChG film. (h) Etching SiO₂.

The key parameters of the waveguide include h_3 and w_1 . h_3 and w_1 influence the limiting effect of slot on light. Therefore, the SiO₂ fabricated by CVD and the ChG strip fabricated by lithography and etching have great influence on waveguide sensor performance. Lithography and etching processes need to be optimized to obtain almost vertical waveguide sidewalls. To reduce

the fabrication error, a more precise mask alignment system and masks can be used according to the optimized fabrication conditions. Every fabrication step should be monitored to characterize the device sample.

4. Waveguide gas sensor characteristics

The output power of ICL (Nanoplus, Germany) is set to 10 mW. A HgCdTe detector (Thorlabs, PDA10JT, USA) is used to obtain the signal from the drop port with an operation wavelength from 2 μm to 5.4 μm , a NEP of 2.08×10^{-11} $\text{WHz}^{-1/2}$ and a B of 160 kHz.

4.1. L_{eff} and DR

Curves of L_{eff} and E versus C are shown in Fig. 8(a). L_{eff} and E become stable and larger than 2.4 cm and 33, respectively, when $C < 1000$ ppm. Curves of $D_1(C)$, $PCF\alpha_{\text{gas}}(C)$ and $-\ln[D_1(C)/D_0]$ versus C under the optimal waveguide parameters are shown in Fig. 8(b). $D_1(C)$ decreases nonlinearly with the increase of C leading to the increase of $-\ln[D_1(C)/D_0]$. But the increase rate of $-\ln[D_1(C)/D_0]$ decreases with the increase of C , and $-\ln[D_1(C)/D_0] < PCF\alpha_{\text{gas}}(C)$ when $C > 66000$ ppm. So with the increase of C , L_{eff} and E gradually decrease, and L_{eff} and E decrease to ~ 0.8 cm and 11.27, respectively, at a pure CH_4 environment.

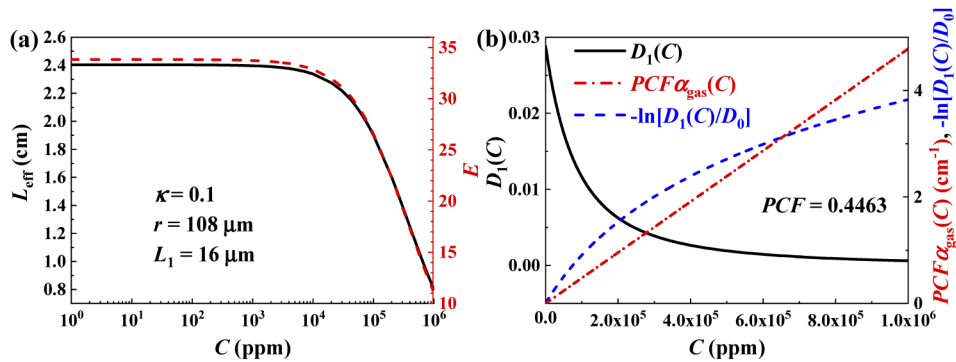


Fig. 8. (a) Curves of L_{eff} and E versus C , where $\kappa = 0.1$, $r = 108 \mu\text{m}$ and $L_1 = 16 \mu\text{m}$. (b) Curves of $D_1(C)$, $PCF\alpha_{\text{gas}}(C)$ and $-\ln[D_1(C)/D_0]$ versus C under the optimal waveguide parameters.

With mature fabrication technique, the intrinsic loss of the ChG rectangular waveguide can satisfy $\alpha_{\text{int}} < 3$ dB/cm [33–35]. In this work, we assume that $\alpha_{\text{int}} = 3$ dB/cm. Based on Eq. (12), the L_0D is calculated to be 3.87 ppm, and the corresponding L_{eff} and E are 2.4 cm and 33.83, respectively. C_{max} is calculated to be 100% according to Eq. (13). Therefore, the DR of the sensor system is [3.87 ppm, 100%].

Curves of the full width at half maximum (FWHM) and quality factor (Q) of the microcavity versus C are shown in Fig. 9. The FWHM and Q decrease with the increase of C because of gas absorption. A lower Q leads to the decrease of L_{eff} as shown in Fig. 8(a). Even though L_{eff} decreases, the increase of C will cause the output power to decrease continuously. However, a larger L_{eff} makes the output power change more obviously with C , and the change rate decreases with the decrease of L_{eff} , causing the drop of the sensitivity.

4.2. Response time

Gas diffusion time determines the response time of the sensor. A detailed procedure for the determination of the response time can be seen in our previous work [28]. Under the condition of static free diffusion, only the gas diffusion process in the horizontal slot region is considered, and

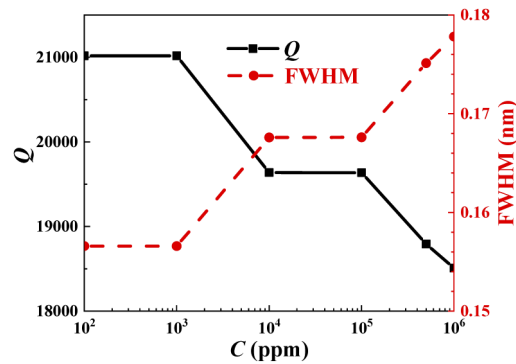


Fig. 9. Curves of the FWHM and Q of the microcavity versus C .

the diffusion time needed in other area is ignored. Through COMSOL Multiphysics simulation, curve of waveguide output power P_1 versus t is shown in Fig. 10(a), where the initial gas concentration in the slot region C_0 is 5000 ppm and the initial concentration in other area C_1 is 0 ppm. The 10%–90% rise time is determined to be 4.5 μ s. Curve of P_1 versus t is shown in Fig. 10(b), where C_0 is 0 ppm and C_1 is 5000 ppm. The 90%–10% fall time is 4.4 μ s.

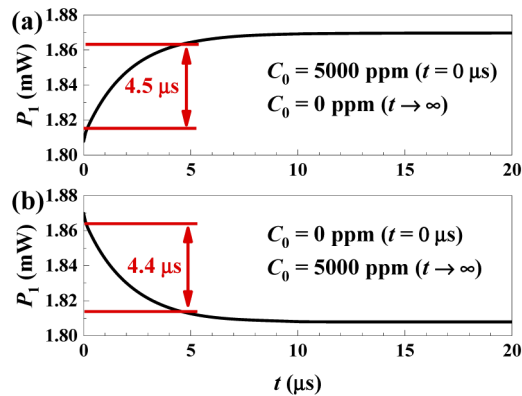


Fig. 10. (a) Curve of P_1 versus t when the initial CH_4 concentration in the slot $C_0 = 5000$ ppm and the initial concentration in other region is 0 ppm. (b) Curve of P_1 versus t when the initial CH_4 concentration in the slot $C_0 = 0$ ppm and the initial concentration in other region is 5000 ppm.

4.3. Influence of environmental pressure variation

The environmental pressure variation will influence the normalized gas absorption coefficient α_{gas} and therefore influence LoD . Curves of α_{gas} and LoD versus gas pressure are shown in Fig. 11(a), where $T = 25$ °C. The increase of pressure leads to the decrease of LoD . However, the variation of LoD is < 1 ppm with a variation of pressure from 0.6 atm to 1.4 atm. So the influence of environmental pressure variation can be ignored.

4.4. Influence of waveguide intrinsic loss

The structure of the ChG/silica-on-fluoride horizontal slot-waveguide is different from conventional ChG rectangular waveguide. Within the range of 1 – 10 dB/cm, curves of E , L_{eff} and LoD versus α_{gas} are shown in Fig. 11(b). With the increase of α_{int} , E and L_{eff} drop. The decrease

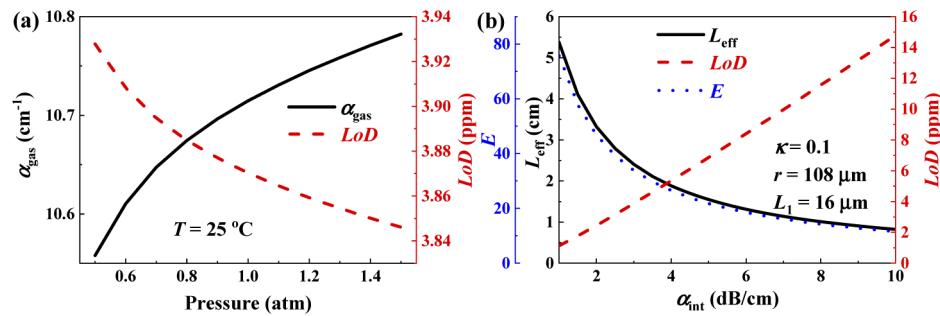


Fig. 11. (a) Curves of α_{gas} and LoD versus environmental pressure, where $T = 25^\circ\text{C}$. (b) Curves of L_{eff} , E and LoD versus α_{int} , where $\kappa = 0.1$, $r = 108 \mu\text{m}$ and $L_1 = 16 \mu\text{m}$.

of P_s leads to the increase of LoD . Though the sensing characteristics become worse, LoD is still < 15 ppm. So the sensor can be used for monitoring CH_4 leakage for safety operation. If α_{int} is reduced to 1 dB/cm, L_{eff} and E can increase to 5.38 cm and 75.7, respectively, and LoD can drop to 1.12 ppm. Therefore, reducing α_{int} is an effective method to improve the sensor performance. The effect of coupling loss on the sensing characteristics is consistent with that of the α_{int} , because they directly affect the output power. The coupling loss decreases the output power, which leads to the increase of the LoD and the decrease of L_{eff} .

4.5. Comparison of PCF among this horizontal slot waveguide and other waveguide structures

Other simulation methods such as finite difference method (FDM) and finite-difference time-domain (FDTD) were reported for calculating PCF . In comparison with these methods, FEM is more precise and consistent with the experimental results [25]. So we use FEM to calculate the PCF of other ChG waveguide structures reported in [19,22–23], and the results are shown in the rightmost column in Table 2. As can be seen, the PCF of the proposed ChG/silica-on-fluoride horizontal slot-waveguide racetrack resonator is at least 5 times larger than other ChG rectangular waveguide. Though the suspended ChG slot waveguide has the largest PCF , its scattering loss is larger than the horizontal slot waveguide due to dry etching. Moreover, the suspended ChG slot waveguide with large PCF is unsuitable to be used in the microring resonator because of large bending loss. The racetrack waveguide reduces the length of the device by more than 30 times when the CH_4 concentration is less than 40000 ppm.

Table 2. Comparison among the proposed sensor and other reported ChG waveguide sensors.

Refs.	L_t (cm)	Waveguide type	λ (μm)	Reported PCF	Simulation method	PCF (FEM ^a)
[22]	1	Rectangular	1.55	5%	FDM	4.61%
[19]	1.7	Rectangular	7.70	5%	FDTD	1.75%
[23]	4.3	Rectangular	4.30	8%	FDTD	3.67%
[28]	1.45	Suspended slot	3.291	85.77%	FEM	85.77%
This paper	0.094	Horizontal slot	3.291	44.63%	FEM	44.63%

^aUsing FEM to calculate the PCF of other reported waveguide structures.

Microring resonators are widely used in refractive index sensing. A refractive index sensor obtains the wavelength drift according to the change of the refractive index of analyte. The sensitivity of a reported refractive index waveguide sensor is $\sim 10^3$ nm/RIU, and the refractive index difference between CH_4 and air is $\sim 4 \times 10^{-4}$, which leads to a wavelength drift of only \sim

0.4 nm for a refractive sensor and the signal variation ($\Delta\lambda/\lambda$) is only $\sim 10^{-4}$. The light intensity decreases exponentially with the increase of gas concentration and the signal variation ($\Delta P/P$) for CH_4 at LoD is $\sim 4 \times 10^{-2}$. So this sensor can make the change of signal more sensitive and the light intensity change is easier to detect through a detector.

Our group proposed a CH_4 sensor with a 16 m multi-pass gas cell (MPGC, physical size: $45 \times 11 \times 11 \text{ cm}^3$, Egold Technology, Wuhan, Hubei Province, China) at the same wavelength and the LoD of this sensor is ~ 43.9 parts-per-billion (ppb) [3]. The waveguide sensor proposed in this paper with a L_{eff} of 2.4 cm can achieve a LoD of 3.87 ppm. The PCF in free-space is 1 and that of our waveguide sensor is 44.63%. The comparison results are shown in Table 3. The low PCF, low L_{eff} and waveguide loss lead to a higher LoD than the free-space CH_4 sensor. But the $\text{LoD} \times L_{\text{eff}}$ of the waveguide sensor is less than that of the free-space CH_4 sensor, which indicates a good performance of the proposed sensor structure.

Table 3. Comparison between free-space CH_4 sensor and this waveguide sensor.

Refs.	P_0	PCF	α_{int}	L_{eff}	LoD	$\text{LoD} \times L_{\text{eff}}$
[3]	4.85 mW	1	0	16 m	~ 43.9 ppb	$\sim 7 \times 10^{-5}$ cm
This paper	10 mW	44.63%	3 dB/cm	2.4 cm	3.87 ppm	$\sim 9.3 \times 10^{-6}$ cm

5. Conclusions

A novel ChG/silica-on-fluoride horizontal slot-waveguide racetrack resonator was proposed for microcavity-enhanced absorption spectroscopic CH_4 sensing. The waveguide structural parameters were optimized for single-mode propagation, large PCF and L_{eff} with a small footprint size. The PCF of the proposed waveguide is 44.63%, which is at least 5 times larger than other reported ChG rectangular waveguides. CH_4 is used for evaluating the sensing characteristics of the sensor. The waveguide length is reduced at least 30 times for compactness of the sensor. The LoD is determined to be 3.87 ppm with an intrinsic waveguide loss of 3 dB/cm. The response time of the sensor is as short as 5 μs owing to the small light-gas interaction area. The variation of environmental pressure has less effect on the sensing characteristics, and a small intrinsic loss is preferred for improving the sensor performances. With a change of resonant wavelength, the proposed ESM, related formulations and analytical methods can also be adopted to the design of a chip-scale waveguide sensor for the detection of other gas species.

Funding

National Natural Science Foundation of China (61604151, 61627823, 61775079, 61960206004); Key Science and Technology R&D program of Jilin Province, China (20180201046GX, 20190101016JH, 20200401059GX).

Disclosures

The authors declare no conflicts of interest.

References

1. C. Zheng, W. Ye, N. P. Sanchez, C. Li, L. Dong, Y. Wang, R. J. Griffin, and F. K. Tittel, "Development and field deployment of a mid-infrared methane sensor without pressure control using interband cascade laser absorption spectroscopy," *Sens. Actuators, B* **244**, 365–372 (2017).
2. B. Li, C. Zheng, H. Liu, Q. He, W. Ye, Y. Zhang, J. Pan, and Y. Wang, "Development and measurement of a near-infrared CH_4 detection system using 1.654 μm wavelength-modulated diode laser and open reflective gas sensing probe," *Sens. Actuators, B* **225**, 188–198 (2016).
3. F. Song, C. Zheng, W. Yan, W. Ye, Y. Wang, and F. K. Tittel, "Interband cascade laser based mid-infrared methane sensor system using a novel electrical-domain self-adaptive direct laser absorption spectroscopy (SA-DLAS)," *Opt. Express* **25**(25), 31876–31888 (2017).

4. M. Dong, C. Zheng, D. Yao, G. Zhong, S. Miao, W. Ye, Y. Wang, and F. K. Tittel, "Double-range near-infrared acetylene detection using a dual spot-ring Herriott cell (DSR-HC)," *Opt. Express* **26**(9), 12081–12091 (2018).
5. Q. He, C. Zheng, M. Lou, W. Ye, Y. Wang, and F. K. Tittel, "Dual-feedback mid-infrared cavity-enhanced absorption spectroscopy for H₂CO detection using a radio-frequency electrically-modulated interband cascade laser," *Laser Phys.* **26**(12), 15436–15444 (2018).
6. X. Yin, H. Wu, L. Dong, B. Li, W. Ma, L. Zhang, W. Yin, L. Xiao, S. Jia, and F. K. Tittel, "ppb-Level SO₂ Photoacoustic Sensors with a Suppressed Absorption–Desorption Effect by Using a 7.41 μm External-Cavity Quantum Cascade Laser," *ACS Sens.* **5**(2), 549–556 (2020).
7. H. Wu, L. Dong, X. Yin, A. Sampaolo, P. Patimisco, W. Ma, L. Zhang, W. Yin, L. Xiao, V. Spagnolo, and S. Jia, "Atmospheric CH₄ measurement near a landfill using an ICL-based QEPAS sensor with V-T relaxation self-calibration," *Sens. Actuators, B* **297**, 126753 (2019).
8. L. Dong, F. K. Tittel, C. Li, N. P. Sanchez, H. Wu, C. Zheng, Y. Yu, A. Sampaolo, and R. J. Griffin, "Compact TDLAS based sensor design using interband cascade lasers for mid-IR trace gas sensing," *Opt. Express* **24**(6), A528–A535 (2016).
9. L. Dong, C. Li, N. P. Sanchez, A. K. Gluszek, R. J. Griffin, and F. K. Tittel, "Compact CH₄ sensor system based on a continuous-wave, low power consumption, room temperature interband cascade laser," *Appl. Phys. Lett.* **108**(1), 011106 (2016).
10. S. Akbar, P. Dutta, and C. Lee, "High-temperature ceramic gas sensors: a review," *Int. J. Appl. Ceram. Technol.* **3**(4), 302–311 (2006).
11. W. Lai, S. Chakravarty, X. Long, C. Lin, and R. Chen, "On-chip methane sensing by near-IR absorption signatures in a photonic crystal slot waveguide," *Opt. Lett.* **36**(6), 984–986 (2011).
12. R. Dwivedi and A. Kumar, "A compact and ultra-high sensitive RI sensor using modal interference in an integrated optical waveguide with metal under-cladding," *Sens. Actuators, B* **240**, 1302–1307 (2017).
13. J. Alaman, M. Lopez-Valdeolivas, R. Alicante, and C. Sanchez-Somolinos, "Optical Planar Waveguide Sensor with Integrated Digitally-Printed Light Coupling-in and Readout Elements," *Sensors* **19**(13), 2856 (2019).
14. T. Jin, L. Li, B. Zhang, H. G. Lin, H. Wang, and P. T. Lin, "Optical-feedback cavity-enhanced absorption: a compact spectrometer for real-time measurement of atmospheric methane," *Sci. Rep.* **7**(1), 5836 (2017).
15. J. Su, "Label-Free Biological and Chemical Sensing Using Whispering Gallery Mode Optical Resonators: Past, Present, and Future," *Sensors* **17**(3), 540 (2017).
16. C. Chen, D. A. Mohr, H. Choi, D. Yoo, M. Li, and S. Oh, "Waveguide-Integrated Compact Plasmonic Resonators for On-Chip Mid-Infrared Laser Spectroscopy," *Nano Lett.* **18**(12), 7601–7608 (2018).
17. D. A. Mohr, D. Yoo, C. Chen, M. Li, and S. Oh, "Waveguide integrated mid-infrared plasmonics with high-efficiency coupling for ultracompact surface-enhanced infrared absorption spectroscopy," *Opt. Express* **26**(18), 23540–23549 (2018).
18. C. Ranacher, C. Consani, A. Tortschanoff, R. Jannesari, M. Bergmeister, T. Grille, and B. Jakoby, "Mid-infrared absorption gas sensing using a silicon strip waveguide," *Sens. Actuators, A* **277**, 117–123 (2018).
19. A. Gutierrez-Arroyo, E. Baudet, L. Bodiou, J. Lemaitre, I. Hardy, F. Fajjan, B. Bureau, V. Nazabal, and J. Charrier, "Optical characterization at 7.7 μm of an integrated platform based on chalcogenide waveguides for sensing applications in the mid-infrared," *Opt. Express* **24**(20), 23109–23117 (2016).
20. B. Kumari, R. K. Varshney, and B. P. Pal, "Design of chip scale silicon rib slot waveguide for sub-ppm detection of N₂O gas at mid-IR band," *Sens. Actuators, B* **255**, 3409–3416 (2018).
21. V. M. Lavchiev and B. Jakoby, "Photonics in the Mid-Infrared: Challenges in Single-Chip Integration and Absorption Sensing," *IEEE J. Sel. Top. Quantum Electron.* **23**(2), 452–463 (2017).
22. J. Charrier, M. L. Brandily, H. Lhermite, K. Michel, B. Bureau, F. Verger, and V. Nazabal, "Evanescent wave optical micro-sensor based on chalcogenide glass," *Sens. Actuators, B* **173**, 468–476 (2012).
23. A. Gutierrez-Arroyo, E. Baudet, L. Bodiou, V. Nazabal, E. Rinnert, K. Michel, B. Bureau, F. Colas, and J. Charrier, "Theoretical study of an evanescent optical integrated sensor for multipurpose detection of gases and liquids in the Mid-Infrared," *Sens. Actuators, B* **242**, 842–848 (2017).
24. D. M. Kita, J. Michon, S. G. Johnson, and J. Hu, "Are slot and sub-wavelength grating waveguides better than strip waveguides for sensing?" *Optica* **5**(9), 1046–1054 (2018).
25. L. Tombez, E. J. Zhang, J. S. Orcutt, S. Kamlapurkar, and W. M. J. Green, "Methane absorption spectroscopy on a silicon photonic chip," *Optica* **4**(11), 1322–1325 (2017).
26. Z. Han, P. Lin, V. Singh, L. Kimerling, J. Hu, K. Richardson, A. Agarwal, and D. T. H. Tan, "On-chip mid-infrared gas detection using chalcogenide glass waveguide," *Appl. Phys. Lett.* **108**(14), 141106 (2016).
27. A. Nitkowski, L. Chen, and M. Lipson, "Cavity-enhanced on-chip absorption spectroscopy using microring resonators," *Opt. Express* **16**(16), 11930–11936 (2008).
28. M. Pi, C. Zheng, R. Bi, H. Zhao, L. Liang, Y. Zhang, Y. Wang, and F. K. Tittel, "Design of a mid-infrared suspended chalcogenide/silica-on-silicon slot-waveguide spectroscopic gas sensor with enhanced light-gas interaction effect," *Sens. Actuators, B* **297**, 126732 (2019).
29. S. Ghosh and B. M. A. Rahman, "Design of on-chip hybrid plasmonic Mach-Zehnder interferometer for temperature and concentration detection of chemical solution," *Sens. Actuators, B* **279**, 490–502 (2019).
30. A. Savchenkov and A. Matsko, "Calcium fluoride whispering gallery mode optical resonator with reduced thermal sensitivity," *J. Opt.* **20**(3), 035801 (2018).

31. D. Kita, H. Lin, J. Li, Z. Han, P. Su, T. Gu, A. Agarwal, A. Yadav, K. Richardson, and J. Hu, "Suspended chalcogenide microcavities for ultra-sensitive chemical detection," *IEEE Sens.* (2016).
32. P. T. Lin, H. G. Lin, Z. Han, T. Jin, R. Millender, L. C. Kimerling, and A. Agarwal, "Label-Free Glucose Sensing Using Chip-Scale Mid-Infrared Integrated Photonics," *Adv. Opt. Mater.* **4**(11), 1755–1759 (2016).
33. X. Gai, S. Madden, D. Y. Choi, D. Bulla, and B. Luther-Davies, "Dispersion engineered $\text{Ge}_{11.5}\text{As}_{24}\text{Se}_{64.5}$ nanowires with a nonlinear parameter of $136\text{W}^{-1}\text{m}^{-1}$ at 1550 nm," *Opt. Express* **18**(18), 18866–18874 (2010).
34. J. F. Viens, C. Meneghini, A. Villeneuve, T. V. Galstian, E. J. Knystautas, M. A. Duguay, K. A. Richardson, and T. Cardinal, "Fabrication and characterization of integrated optical waveguides in sulfide chalcogenide glasses," *J. Lightwave Technol.* **17**(7), 1184–1191 (1999).
35. X. Gai, D. Y. Choi, S. Madden, and B. Luther-Davies, "Polarization-independent chalcogenide glass nanowires with anomalous dispersion for all-optical processing," *Opt. Express* **20**(12), 13513–13521 (2012).